Changes in TOA SW Fluxes over Marine Clouds When Estimated via Semi-Physical Angular Distribution Models

F. Tornow[1,2,3*] C. Domenech[4], J. N. S. Cole[5], N. Madenach[1], J. Fischer[1]

[1] *Institute for Space Sciences, Freie Universität Berlin, Berlin, Germany*

[2] *Earth Institute, Columbia University, New York, NY, USA*

[3] *NASA GISS, New York, NY, USA*

[4] *GMV, Madrid, Spain*

[5] *Environment and Climate Change Canada, Toronto, Canada*

[*] *Corresponding author*: Florian Tornow, Center for Climate Systems Research, Earth Institute, Columbia University, 2880 Broadway New York, NY 10025

ABSTRACT

Top-of-atmosphere (TOA) shortwave (SW) angular distribution models (ADMs) approximate – per angular direction of an imagined upward hemisphere – the intensity of sunlight scattered back from a specific Earth-atmosphere scene. ADMs are, thus, critical when converting satellite-borne broadband radiometry into estimated radiative fluxes. This paper applies a set of newly developed ADMs with a more refined scene definition and demonstrates tenable changes in estimated fluxes compared to currently operational ADMs. Newly developed ADMs use a semi-physical framework to consider cloud-top effective radius, $\overline{R}_e$, and above-cloud water vapor, $ACWV$, in addition to accounting for surface wind speed and clouds' phase, fraction, and optical depth. In effect, instantaneous TOA SW fluxes for marine liquid-phase clouds had the largest flux differences (of up to 25 W m^{-2}) for lower solar zenith angles and cloud optical depth greater than 10 due to extremes in $\overline{R}_e$ or $ACWV$. In regions where clouds had persistently extreme levels of $\overline{R}_e$ (here mostly for $\overline{R}_e$<7μm and $\overline{R}_e$>15μm) or $ACWV$, instantaneous fluxes estimated from Aqua, Terra, and Meteosat 8 and 9 satellites using the two ADMs differed systematically, resulting in significant deviations in daily mean fluxes (up to ±10 W m^{-2}) and monthly mean fluxes (up to ±5 W m^{-2}). Flux estimates using newly developed, semi-physical ADMs may contribute to a better understanding of solar fluxes over low-level clouds. It remains to be seen whether aerosol indirect effects are impacted by these updates.

1. Introduction

Clouds reflect and absorb sunlight and, thus, crucially modify how much light reaches the surface, which atmospheric vertical levels experience heating from light absorption, and how much light eventually leaves the Earth-atmosphere-system through the top-of-atmosphere (TOA). Representing cloud reflection and absorption in climate models is challenging as both processes are function of the amount and phase of cloud condensate, its micro-physical character (Twomey 1977), and its inhomogeneous three-dimensional structure (Cahalan et al. 1994; Barker et al. 1996; Hogan et al. 2019). This complexity, combined with the need for computationally efficient radiative transfer calculations require climate models to make simplifying assumptions (e.g. Fu and Liou 1992; Clough et al. 2005; Bender et al. 2006; Pincus et al. 2003). The benchmark to assess the realism of a climate models' radiative response is TOA radiative fluxes (Ramanathan 1987; Bony et al. 1992; Li et al. 2013) as they can be estimated from many satellites that have been sampling vast regions frequently for more than 50 years (Dewitte and Clerbaux 2017).

Marine boundary-layer clouds are particularly relevant as they – and their relatively high albedo – replace an otherwise dark (i.e. low albedo) ocean surface. These clouds are potentially exposed to natural and anthropogenic sources of aerosol such as biomass burning events closer to continents (Painemal et al. 2014) or ship exhaust along merchant routes (e.g. Toll et al. 2017). Acting as cloud condensation nuclei, aerosol can redistribute cloud condensate locally towards more numerous, smaller droplets that reflect sunlight more efficiently (Twomey 1977). Ensuring that we understand the cloud radiative effect of boundary-layer clouds is important, as their dynamics and therefore their temporal evolution is in large part determined by cloud-top radiative cooling (Lilly 1968; Wood 2012).

To estimate TOA solar fluxes from satellite observations, three components are required: 1) knowledge of the underlying scene properties of surface and atmospheric constituents which are usually retrieved from an on-board multi-spectral imager or collocated from auxiliary data sets if irretrievable; 2) broadband radiance that is either inferred from narrow multi-spectral channels across the solar spectrum or preferably measured via an on-board broadband radiometer; and 3) a carefully designed model with assumptions about how solar radiation will be scattered into different angular directions of an imagined upward hemisphere so that the broadband radiance, measured at one angular direction can be transformed into a broadband flux (Suttles et al. 1988; Smith et al. 1986; Loeb et al. 2003, 2005; Su et al. 2015). The angular variation of reflected solar radiation is referred to as anisotropy and can vary considerably across scenes and sun-observer geometries. For clouds over ocean (the central topic of this study) any scene with a cloud fraction smaller than 100% may encompass specular reflection from the water surface that changes the intensity and angular distribution as higher surface wind speeds roughen the surface and create tilted reflecting facets (Cox and Munk 1954). Overcast cloudy scenes distribute sunlight differently with cloud optical depth as increased multi-scattering leads to a more Lambertian-like reflection (e.g. Gao et al. 2013). Tornow et al. (2020) developed a method to incorporate cloud micro-physical characteristics (represented through cloud-top effective radius $\overline{R}_e$) and amount of absorbing above-cloud water vapor ($ACWV$) into anisotropy-predicting angular distribution models (ADMs).

Any ADM development that further refines the definition of Earth-atmosphere scenes, and therefore enables consideration of additional effects impacting anisotropy, warrants a look at how resulting flux estimates compare against the current standard (demonstrated briefly for past ADM developments in e.g. Su et al. 2015). And as newly estimated fluxes are potentially more accurate and may help the community improve their understanding of cloud-aerosol-radiation interaction, newly developed ADMs have not only been applied to upcoming satellite missions but also to the existing wealth of past and current satellite observations. For example, such development-driven reprocessing led to several versions of the widely used CERES SSF (Cloud and Earth's Radiant Energy System Single Scanner Footprints) data product (e.g. Smith et al. 2011, or as documented in https://ceres.larc.nasa.gov/data/documentation/#historical-editions_).

This study makes a case for newly developed, semi-physical ADMs to be considered as the next-generation solution and to refine flux estimates in past, current, and future missions. We investigated whether TOA shortwave (SW) fluxes are significantly different when using currently operational ADMs, employed in most-recent CERES SSF Edition 4A (Loeb et al. 2005; Su et al. 2015), versus newly developed, semi-physical ADMs (Tornow et al. 2020). Analysis of instantaneous flux estimates found differences of up to 25 W m^{-2} in cases of extremes in $\overline{R}_e$ and $ACWV$. To investigate impacts across larger regions and longer time scales, we processed two months of polar-orbiting and geostationary satellite observations over the tropical and southern Atlantic where there are often low-level clouds (e.g. Cesana et al. 2019) of varying microphysical properties (e.g. Bennartz and Rausch 2017) as well as above-cloud water vapor. Daily and monthly mean fluxes indicate that systematic instantaneous differences between the ADMs can propagate into time means with significant differences of up to 10 W m^{-2} for daily means and up to 5 W m^{-2} for monthly means.

This paper is organized as follows. Section 2 introduces ADMs, their estimated uncertainty, and the satellite data used as input for the ADMs. Section 3 presents our main results and Section 4 discusses them.

2. Materials and Methods

The following subsections explain the fundamentals of currently operational as well as newly developed, semi-physical ADMs and how we obtained anisotropy from them (Sec. 2a), the way we approximate uncertainty of flux estimates (Sec. 2b), and the satellite observations we used as input for both ADMs (Sec. 2c).

a. Empirical Angular Distribution Models for Marine Clouds

Empirical ADMs describe the expected angular distribution of sunlight reflected back towards TOA based on CERES-MODIS observations (Wielicki et al. 1996) collected over a 5-year period (2000-2005) by taking measurements using a rotational azimuth plane scan mode. An imagined upward hemisphere was discretized into 2° angular elements, forming an angular bin per joint combination of solar zenith angle θ_0, viewing zenith angle θ_v, and relative azimuth angle φ interval (their intervals denoted by superscript Δ generally or by letters when pointing at specific intervals). For each angular bin, available CERES SSF (described in more detail in Section 2c) samples were used to train the currently operational, sigmoidal approach (Loeb et al. 2005; Su et al. 2015) described in Sec. 2a1, and newly developed, semi-physical approach (Tornow et al. 2020) discussed in Sec. 2a2 – each striving to minimize residuals between radiance-predicting models and CERES-MODIS observations. The key difference between the two approaches is scene definition and parameters used to define a scene that may result in different TOA SW anisotropies for the same set of measurements. We reproduced the currently operational CERES approach to ensure consistent fusion with simulated radiances (Sec. 2a3) and coherent anisotropy estimation (Sec. 2a4).

1) Currently operational ADMs using sigmoidal fits

Footprint level data from the CERES SSF were first classified into groups of MODIS-retrieved cloud phases: ice phase, liquid phase, and mixed phase. Note that CERES SSF footprints can contain a layer of ice and a layer of liquid condensate with some horizontal displacement so both layers are visible from space. Per cloud phase, scenes were defined in a continuous manner through the product of layer cloud optical depth $\tilde{\tau}$ (the exponential of the average over logarithmic τ values over a cloud layer retrieved by MODIS) and cloud fraction f. A sigmoid curve was used to fit CERES-observed radiances I and the parameter $x = \log \tilde{\tau} f$ which is based on MODIS retrievals

$$I(\theta_0^\Delta, \theta_v^\Delta, \varphi^\Delta) = I_0 + \frac{a}{\left[1 + e^{-\frac{(x-x_0)}{b}}\right]^c} \tag{1}$$

where I_0, a, b, c, and x_0 were free parameters.

In case of low cloud fraction or low optical thickness ($x < 6$) and viewing geometries potentially affected by sun-glint (i.e. sun-glint angles < 20°), a look-up-table for that angular bin stored the average of observed TOA SW radiances per interval of x (intervals: <3.5, 3.5-4.5, 4.5-5.5, 5.5-6) and 10 m wind speed (intervals: 0-2, 2-4, 4-6, 6-8, 8-10, and > 10 m s^{-1}). This approach is currently used in CERES SSF Edition 4A to estimate fluxes (Su et al. 2015).

2) Newly developed, Semi-Physical Approach

Like the currently operational CERES approach (Sec. 2a1), cloudy footprints were separated by their phase and scene definition was a continuous function of the following parameters. Per cloud phase, a semi-physical approach served to define scenes via a footprint albedo α and via an absorption through above-cloud water vapor $ACWV$. The footprint albedo incorporated each footprint's clear portion (that involved a clear-sky albedo α^{ocean} as well as potential sun-glint contribution r^{SunGlint} predicted from a Cox-Munk model using 10 m wind speed) as well as up to two cloudy portions (each with a statistically predicted two-stream cloud albedo $\alpha_{1,2}^{\text{TwoStream}}$ using MODIS-retrieved $\tilde{\tau}_{1,2}$, $\overline{R}_{\text{e},1,2}$) together weighted by their respective cloud fraction. This approach was used in its log-linear form for ordinary least square fitting to CERES-MODIS observations to find optimal, free parameters A, B, and C:

$$\log I(\theta_0^\Delta, \theta_v^\Delta, \varphi^\Delta) \approx A + B \cdot \log \alpha + C \cdot ACWV \tag{2}$$

With footprint albedo α

$$\alpha = f_0 \cdot (\alpha^{\text{ocean}} + r^{\text{SunGlint}}) + f_1 \cdot \alpha_1^{\text{TwoStream}} + f_2 \cdot \alpha_2^{\text{TwoStream}} \tag{3}$$

and using the functional form of the two-stream cloud albedo $\alpha^{\text{TwoStream}}$ to ingest MODIS-inferred $\tilde{\tau}$ and $\overline{R}_e$:

$$\alpha^{\text{TwoStream}} = \frac{\alpha^{\text{ocean}} + (1-\alpha^{\text{ocean}})(1-g)\tilde{\tau}/2}{1 + (1-\alpha^{\text{ocean}})(1-g)\tilde{\tau}/2} \tag{4}$$

To capture observations best, two additional optimization steps were performed: 1) instead of a fixed asymmetry parameter $g(\overline{R}_e)$ in the two-stream albedo (Eq. 4) we allowed variation with sun-observer-geometry and found optimal $g(\overline{R}_e)$ through an approximation of $g(\overline{R}_e) = a + b \cdot \overline{R}_e + c \cdot \overline{R}_e^2$ and an exhaustive search of the a-b-c parameter space; 2) for least-square fitting (Eq. 2) and $g(\overline{R}_e)$ optimization we only used horizontally homogeneous clouds (i.e. a $\nu = \left(\frac{\overline{\tau}}{\sigma(\tau)}\right)^2 > 10$) of high MODIS retrieval quality (>80% of pixel within the cloud layer reported as well-retrieved) to avoid sampling biases and maximize consistency of predicted radiances across angular bins. We performed step 1 first for footprints of pure liquid and ice clouds so that we could use optimized $g(\overline{R}_e)_{\text{liq}}$ and $g(\overline{R}_e)_{\text{ice}}$ for footprints of mixed phase. Tornow et al. (2020) provide more details on this methodology and also explain that alternative approaches, such as separate sigmoidal fitting over subsets of CERES-MODIS data defined by $\overline{R}_e$ and $ACWV$ intervals, may be infeasible due to partially sparse sampling of $\overline{R}_e$ and $ACWV$.

3) Use of Radiative Transfer Simulations

Observations covered between 71-98% of sun-observer-geometries (for $\theta_0 > 20°$, Table 3 in Tornow et al. 2020). To produce complete hemispheric fields of upwelling TOA SW radiances we used the plane-parallel radiative transfer code MOMO (Matrix Operator Model, Hollstein and Fischer 2012) to simulate solar radiances. MOMO has foremost been applied to narrow-band retrievals (e.g. Lindstrot et al. 2009; Diedrich et al. 2013) and was adapted to simulate the solar spectrum through 53 separate spectral intervals covering 0.25 – 4.0µm, each using non-correlated k-binning (Bennartz and Fischer 2000) based on HITRAN-2008 (Rothman et al. 2009). Liquid-phase clouds were represented through sub-adiabatic prototypes (e.g. Brenguier et al. 2000) over up to 18 vertical layers and covered cloud optical depths between 0.3 and 27.1, cloud-top effective radii between 4.7 and 30.1µm and above-cloud water vapor between 3.3 and 39.1 kg m^{-2}. Phase functions of liquid cloud droplets were calculated via Mie theory. For ice clouds, we used a single layer at higher altitude and produced optical depth ranges between 1 and 50, ice crystal effective radii between 20 and 50µm, and above-cloud water vapor between 0.32 and 0.33 kg m^{-2}. Phase functions of ice crystals with a General Habit Mixture and severely roughened were extracted from the data base of Baum et al. (2011, 2014). To cover ranges in above-cloud water vapor, we used four different radiosonde vertical profile that represented moisture conditions over a 12 month-period well (see Fig. 2 in Tornow et al. 2018). In order to produce radiances for mixed phase clouds, we linearly combined liquid and ice cloud radiances.

The resulting radiances were interpolated onto a 2° angular grid. To produce consistent fields when joined with observation-based radiances $\bar{I}$ (predicted from either model), simulated radiances I^{sim} were empirically adjusted. Adjustment factors were determined from hemispheric portions captured by observations (denoted as k and l for viewing zenith and relative azimuth angles, respectively) and, then, applied to all other angular portions (denoted as p and q, respectively). The empirical adjustments stem from Loeb et al. (2003) and was applied separately for currently operational and for newly developed, semi-physical ADMs.

$$\hat{I}(\theta_0^i, \theta_v^p, \varphi^q) = \frac{1}{mn} \sum_{k=1}^{m} \sum_{l=1}^{n} \bar{I}(\theta_0^i, \theta_v^k, \varphi^l) \frac{I^{\mathrm{sim}}(\theta_0^i, \theta_v^p, \varphi^q)}{I^{\mathrm{sim}}(\theta_0^i, \theta_v^k, \varphi^l)} \tag{5}$$

Lastly, adjusted simulated radiances $\hat{I}$ served to as input to fit currently operational and newly developed, semi-phyiscal models for angular bins without observations.

4) Extracting Anisotropy

For each set of currently operational and newly developed, semi-physicals ADMs, we joined radiance-predicting models from observations and simulations. To ensure that hemispheric radiance fields were consistent and to avoid outliers from poor statistical or semi-physical observation-based fits, we screened for fits that had residuals with absolute biases lower than 1.5 W m^{-2} sr^{-1} as well as standard deviations smaller than 10 W m^{-2} sr^{-1} (or 50 W m^{-2} sr^{-1} for sun-glint angles smaller 20°) and additionally set a minimum number of CERES-MODIS samples per angular bin (1000 for liquid and mixed-phase, 100 for ice phase). Bins with fewer observations or larger residuals relied entirely on simulated radiances.

Merged models produced radiances over half-hemispheres that were integrated to fluxes using an analytic solution of the integral discretized from $\int_0^{2\pi}\int_0^{\pi/2} I\cos\theta_v\sin\theta_v d\theta_v d\varphi$:

$$\bar{F}(\theta_0^i) = \sum_{k=1}^{m}\sum_{l=1}^{n} \bar{I}(\theta_0^i, \theta_v^k, \varphi^l)[\sin^2(\theta_v^k + 1) - \sin^2(\theta_v^k - 1)]\Delta\varphi \tag{6}$$

Finally, we extracted anisotropy $\bar{R}$ as follows:

$$\bar{R}(\theta_0^i, \theta_v^k, \varphi^l) = \frac{\bar{I}(\theta_0^i, \theta_v^k, \varphi^l)\pi}{\bar{F}(\theta_0^i)} \tag{7}$$

In line with the current CERES methodology (pers. comm. Wenying Su) we performed a reference level correction (Loeb et al. 2002) that accounts for limb brightening as the intercept point is raised from the surface level to some altitude h (here h = 20km) and adjusted the anisotropy as follows (Loeb et al. 2003), where r_e = 6371km is Earth's radius:

$$R(\theta_0^i, \theta_v^k, \varphi^l) = \bar{R}(\theta_0^i, \theta_v^k, \varphi^l)\left(\frac{r_e}{r_e + h}\right) \tag{8}$$

This step amplified all fluxes by 0.3% and did not impact the comparison of estimated fluxes from both ADMs.

Finally, this anisotropy was used to convert the instantaneously-observed radiance I into a flux $\hat{F}$:

$$\hat{F}(\theta_0) = \frac{I(\theta_0, \theta_v, \varphi) \cdot \pi}{R(\theta_0^i, \theta_v^k, \varphi^l)} \tag{9}$$

b. Estimating Uncertainty

To approximate the uncertainty behind each instantaneous flux estimate, we propagated the standard deviation of model fits $\Delta I = \sigma(dI)$, where dI are residuals from fitting of observations or simulations via currently operational or newly developed, semi-physical approach, into flux integrals ΔF and anisotropy estimates ΔR:

$$\Delta F(\theta_0^i) = \sqrt{\sum_{k=1}^{m} \sum_{l=1}^{n} \Delta I^2(\theta_0^i, \theta_v^k, \varphi^l)[\sin^2(\theta_v^k + 1) - \sin^2(\theta_v^k - 1)]\Delta\varphi} \tag{10}$$

as well as

$$\Delta R(\theta_0^i, \theta_v^k, \varphi^l) = R(\theta_0^i, \theta_v^k, \varphi^l)\sqrt{\left(\frac{\Delta I}{\bar{I}}\right)^2 + \left(\frac{\Delta F}{\bar{F}}\right)^2} \tag{11}$$

The relative anisotropy uncertainty was then applied to instantaneous flux estimates:

$$\Delta\hat{F}(\theta_0) = \hat{F}(\theta_0)\frac{\Delta R(\theta_0^i, \theta_v^k, \varphi^l)}{R(\theta_0^i, \theta_v^k, \varphi^l)} \tag{12}$$

Uncertainties of daily and monthly flux averages $\Delta\bar{\bar{F}}$ were calculated as follows, where s is the number of samples:

$$\Delta\bar{\bar{F}} = \sqrt{\frac{1}{s}\sum_{d=1}^{s} \Delta\hat{F}_d^2} \tag{13}$$

Uncertainties from co-registration with auxiliary data, radiance unfiltering, or calibration were not incorporated. To determine whether fluxes from both ADMs and collected over diurnal and monthly time scales differed significantly we also used Student's t-test. To assess their mean difference we also calculated standard errors.

c. Satellite Observations and collocated Parameters

The current operational and newly developed, semi-physical ADMs were applied to inputs for the month of January and July 2007 from CERES SSF Edition4A (Su et al. 2015) of the polar-orbiting Aqua and Terra satellites (FM3 and FM1 instrument, respectively) and GERB Edition 1 (Dewitte et al. 2008) from the geostationary Meteosat-8 (January) and Meteosat-9 (July) satellites. We filtered footprints for water surfaces only in the region bound by 60°S-30°N and 60°W-25°E and for solar geometries of $\theta_0 < 82°$. As briefly introduced in Sec. 1, in this region there are often low-level clouds of a wide range of cloud microphysical properties that arise from varying distances to continents acting as a source of aerosol and a large span in above-cloud water vapor facilitated by latitudinal slopes in precipitable water.

CERES SSF footprints cover approximately 20 km at nadir and solar channels measure the solar radiance over the spectral range of 0.3-5.0 µm. During the time period the CERES instruments operated in cross-track mode sampling Earth homogeneously (Barkstrom 1990). As part of the SSF data set, statistics of MODIS-retrieved cloud properties (∼1 km resolution) were produced for up to two cloud layer per CERES footprint (given their cloud-top pressure differed by at least 50hPa). Statistics include cloud layer averages of effective radius $\overline{R}_e$, cloud-top pressure $\bar{p}^{\mathrm{ctop}}$, and visible cloud optical depth $\bar{\tau}$ as well as additional statistics on cloud optical depth including layer standard deviation of optical depths $\sigma(\tau)$ and the exponential of the average over logarithmic values of cloud optical depth $\tilde{\tau}$, and clear and cloudy fractions, f_0 and $f_{1,2}$, respectively. Wind speed at 10 m provided with the SSF dataset were extracted from GEOS (Goddard Earth Observing System) version 5.4.1 (Rienecker et al. 2008). In order to apply the novel ADMs, we extracted above-cloud water vapor $ACWV$ for each CERES FOV by collocating vertical profiles of temperature $T(p)$ and relative humidity $rh(p)$ from ERA-20C (Poli et al. 2016) via nearest neighbor interpolation accounting for MODIS-detected cloud-top height (of the layer with larger fraction):

$$ACWV = \frac{1}{g}\int_{p^{ctop}}^{0} mr(p,T,rh)dp = \frac{1}{g}\int_{p^{ctop}}^{0} \frac{e_s(T)}{p}\frac{mol_{h20}}{mol_{air}} rh(p)dp \tag{14}$$

with mixing ratio $mr(p,T,rh)$, saturation vapor pressure $e_s = 6.112e^{\frac{17.67T}{T+243.5}}$ (using T in degree Celsius, Bolton 1980), gravitational acceleration g, and molecular weights of water and dry air mol_{h_2o} and mol_{air} respectively. Using radiosonde data from St. Helena from 4 month in 2003, we determined that ERA20C-based ACWV values agreed to within -1.06 ± 4.35 kg m^{-2}. Currently operational CERES TOA SW fluxes were estimated using the sigmoidal approach (Sec. 2a1), as described in Su et al. (2015).

Data from GERB had a footprint size of approximately 10 km at nadir and the instrument's solar channel covered 0.32-4.0 µm. Although data was available every 15 minutes, we decided to process it hourly, with some timeslots missing at the time of acquisition (downloaded Feb. 2019 from `ftp://oma.gerb.be`). Retrieved cloud properties from the multi-spectral imager SEVIRI (circa 3 km pixel size at subsatellite point) include cloud fraction f and visible cloud optical thickness $\tilde{\tau}$, as described above for CERES SSF. Cloud properties from SEVIRI were adjusted to match MODIS-retrieved properties to ensure coherent scene definition (Ipe et al. 2004). To apply newly developed, semi-physical ADMs, we extracted additional SEVIRI parameters from the Cloud Physical Property (CPP) data set version CLAAS 2.0 (Finkensieper et al. 2016; Benas et al. 2017): R_e, cloud phase, p^{ctop} and f at pixel-level. This allowed production of phase-specific layer average optical thicknesses and cloud fractions that we adjusted so that their sum would correspond to GERB values which were paired with layer-averaged effective radii and cloud-top pressure. As above, we used ERA-20C vertical profiles and SEVIRI cloud-top pressure to derive each FOV's $ACWV$ and additionally extracted 10 m wind speed from ERA-20C. Applying the same ADMs to radiometers with slightly shifted spectral coverage inherently assumes proper radiance unfiltering as well as negligible change in actual anisotropic behavior. Note that original GERB processing used older ADMs (Loeb et al. 2003), and application of currently operational or newly developed, semi-physical ADMs may cause deviations from official flux estimates that were not investigated here.

To obtain complete diurnal cycles of TOA SW fluxes (as captured by e.g. Rutan et al. 2014; Gristey et al. 2018) and fill temporal and spatial gaps (due to $\theta_0 > 82°$, missing time slots, and faulty scan lines), we used the CERES SYN1deg-1hour data set (DOI: `10.5067/TERRA+AQUA/CERES/SYN1DEG-1HOUR_L3.004A`) from January and July 2007 as a complement. As described in Doelling et al. (2013, 2018), flux estimates in SYN1deg were a composite based on measurements from multi-spectral imagers onboard geostationary satellites and broadband radiometers from polar-orbiting Aqua and Terra satellites, and GERB was used for validation in that study. Daily and monthly mean cloud properties were taken from the CERES-SYN1deg-day (DOI: `10.5067/Terra+Aqua/CERES/SYN1degDAY_L3.004A`) and CERES-SYN1deg-month (DOI: `10.5067/Terra+Aqua/CERES/SYN1degMonth_L3.004A`) products.

3. Results

Angular distribution models provide crucial knowledge to transform a satellite-perceived TOA SW radiance paired with underlying scene properties into an outgoing TOA SW flux. A newly developed ADM based on semi-physical models (Sec. 2a2) expanded the list of properties defining cloudy scenes over ocean and may, thus, produce significantly different flux estimates compared to the currently operational methodology, introduced as sigmoidal model (Sec. 2a1). In order to verify significance and understand differences, we started by analyzing the impact onto instantaneous flux estimates (Sec. 3a) and, then, examined spatial and temporal flux averages (Sec. 3b).

a. Impact on Instantaneous Flux Estimates

To investigate whether instantaneous flux estimates significantly change when switching from currently operational to newly developed, semi-physical models, we predicted radiance fields from each model and derived anisotropies for three cases of liquid-phase clouds over ocean (Fig. 1). Each case (separated by panel) was further stratified by varying a newly incorporated property which the currently operational approach was insensitive to: cloud-top effective radius $\overline{R}_e$ (Fig. 1, panels I and II) and above-cloud water vapor $ACWV$ (Fig. 1, panel III). Values were chosen to roughly represent the outer margins (red and blue) and most frequent values (green) of observed spectra (exemplary histograms shown in lower panels of Fig. 2). Anisotropy fields were characterized by cloud scattering features, such as cloud bow and cloud glory, as well as sun-glint (for a broken cloud field in Fig. 1, panel II). Anisotropy deviations between ADMs were generally within the uncertainty range, except for angular portions in the backscattering direction (Fig. 1, panel I).

[Figure 1]

For varying $\overline{R}_e$ (Fig. 1, panels I and II), anisotropies exhibit systematic differences in the backscattering region, such that larger droplet sizes caused reduced anisotropies (θ_v between -60° and 0°), a sharper response around the cloud glory (θ_v between -31° and -35°), and a cloud bow shifted further away from the cloud glory (θ_v between -63° and +7°). These systematic deviations in the backscattering region were consistent with Mie-calculated single-scattering intensities (cf. Fig. 1 in Tornow et al. 2018). The anisotropy response to $ACWV$ affected predominantly the forward-scattering direction and will be discussed in the Sec. 4.

[Figure 2]

To understand for which scene properties both ADMs agree, we selected three viewing geometries for solar illumination $\theta_0 \in [32, 34°]$ and two cloud optical thicknesses and varied $\overline{R}_e$ and $ACWV$.

Fig. 2 illustrates where currently operational ADMs (shown as circle) that were insensitive to these variations intersected newly developed, semi-physical ADMs (shown as triangles). For $\overline{R}_e$ (left panel of Fig. 2), the intercepts were found mostly between 10 and 15 μm and correspond to most prevalent values of CERES-MODIS data (shown in histograms in the bottom left panel) that were used to train both sets of ADMs. As shown across three $\tilde{\tau}$ groups, most frequent $\overline{R}_e$ can marginally shift. And as analyzed during ADM development, $\overline{R}_e$ median values across angular bins of the same upward hemisphere can vary substantially (between 7 and 17 μm for selected θ_0, shown in Table 3 of Tornow et al. 2020). For ranging $ACWV$ (right panel of Fig. 2) the anisotropy response was lower and we found fewer matches between ADMs. Missing matches for ranging $ACWV$ could be caused by picking a single $\overline{R}_e$ in this analysis that – as we listed above – could deviate sufficiently from median $\overline{R}_e$ in individual angular bins to which currently operational ADMs may have been biased. For selected scenes and viewing geometries, the shading highlights 5 W m^{-2} flux deviation that could be facilitated by deviations of ±5 μm or ±15 kg m^{-2} from $\overline{R}_e$ and $ACWV$ intercepts, respectively. Note that – because anisotropy integrates by definition to 1 over the upward hemisphere – negative anisotropy differences in one viewing direction must be balanced by positive differences in another direction, and vice versa. Consequently, for the same scene but different viewing geometries, two ADMs can produce flux differences of opposite sign across geometries. This can be seen from different slopes in forward and backscattering direction, for example.

[Figure 3]

To more accurately quantify the impact on resulting flux estimates, we predicted radiance fields $\bar{I}$ using newly developed, semi-physical models (sensitive to $\overline{R}_e$ and $ACWV$) applied anisotropies from both semi-physical and currently operational models, and measured their difference:

$$\delta\hat{F} = \hat{F}_{\text{loglinear}} - \hat{F}_{\text{sigmoidal}} = \frac{\bar{I}\pi}{R_{\text{loglinear}}} - \frac{\bar{I}\pi}{R_{\text{sigmoidal}}} \tag{15}$$

Fig. 3 presents the expected flux difference $\delta\hat{F}$ for two settings of solar geometry and cloud optical depth (by row) as well as cloud micro-physical setup (by column). Given the observer's perspective (defined by θ_v and φ), magnitude and sign of $\delta\hat{F}$ vary considerably. For either small or large droplets sizes (left or right panels of Fig. 3), cloud bow features stand sharply out from cloud glory and were of opposite sign but comparable magnitude. Nadir and forward scattering regions were equally intense and of alternating sign but showed more gradual changes in $\delta\hat{F}$ across viewing geometries. An effective radius of 10 μm had much reduced $\delta\hat{F}$ – possibly the result of median conditions being reflected in currently operational models, as demonstrated above – although some angular portions showed persistent differences (e.g. nadir directions of $\tau = 5.5$ and $\theta_0 = [40°,42°]$ had positive differences regardless of $\overline{R}_e$). Flux differences for various $ACWV$ scenarios (not shown) marked a pronounced response in the forward scattering direction (with positive flux differences for high $ACWV$ values) and a less intense response of opposite sign in the backscattering portion.

[Figure 4]

To quantify an expected upper bound of instantaneous flux changes due to a switch in ADMs and to exclude systematic differences, we took hemispherically resolved flux differences of extreme scenarios (e.g. the left and right column of Fig. 3 for $\overline{R}_e$), measured the span in $\delta\hat{F}$ per angular portion across extremes, and from absolute values divided by 2 (assuming that median conditions of zero difference were roughly centered between extremes) we extracted the 95$^{\text{th}}$ percentile:

$$\delta\hat{F}_{\max} = 95^{\text{th}}\text{percentile of}\frac{|\delta\hat{F}_{20\mu m} - \delta\hat{F}_{5\mu m}|}{2} \tag{16}$$

We repeated quantification for a range of cloud optical depths and solar geometries. Fig. 4 shows how the upper bound was generally within 25 W m^{-2}. For extremes in $\overline{R}_e$, expected flux differences increased with τ up to 10-20 then decreased for $\tau > 20$. This was likely a result of both an increasing cloud albedo and the diminished fraction of single-scattering versus multi-scattering events (thus reducing the dominance of cloud bow and glory features) that are both associated with larger τ. Maxima (at τ of 10-20) grew larger in $\delta\hat{F}_{\max}$ for lower θ_0, as more downwelling radiation reached the cloud for reflection. Accounting for increased solar influx for lower solar zenith angles, resulting peak albedo changes were roughly comparable and amounted to 0.015-0.020. Maxima shifted towards larger τ for lower θ_0; likely the result of more single-scattering features (i.e. cloud bow and cloud glory) positioned closer to the nadir and rather influencing the intensity fields for higher τ values. For extremes in $ACWV$, we found a rising impact with larger τ and lower θ_0. We conclude that increased water vapor absorption effects, associated with $ACWV$, occurred for more available solar radiation (lower θ_0) and higher albedos (larger τ).

[Figure 5]

b. Impact on Daily and Monthly Averages

Figure 3 indicated that regions of persistently low or high $\overline{R}_e$ could repeatedly experience flux differences of similar magnitude and sign when observed under similar viewing geometry over the course of a day (i.e. varying θ_0 and possibly varying τ, but comparable φ and θ_v, e.g. by geostationary platforms) or over the course of a month (e.g. by polar-orbiting satellites). This suggests that temporal and spatial averages of such regions could result in systematic flux differences. To investigate whether flux estimates from newly developed, semi-physical ADMs and their difference to currently operational estimates affect daily and monthly averages, we processed two months (January and July 2007) of CERES-MODIS and GERB-SEVIRI (Sec. 2c) data over the tropical and southern Atlantic (all water surfaces between 60°W and 25°E as well as 60°S and 30°N). Processing involved application of currently operational ADMs (thus reproducing values in CERES-MODIS and upgrading GERB-SEVIRI data, see Sec. 2c) and of newly developed, semi-physical ADMs. Following Doelling et al. (2013), we first averaged fields onto an equal-area grid. An example is shown in Fig. 5 for orbits of Aqua and Terra as well as a time slot of MSG. Flux estimates across missions resulted in roughly similar flux difference pattern in magnitude and sign and could be associated with $\overline{R}_e$ (e.g. the around 12°W and 25°S). Each pixel was then adjusted so GERB fluxes matched with coincident CERES-based estimates. This step assumed an absolute calibration differences between both instruments (Doelling et al. 2013). Figure 6 shows examples of pixels before the GERB-to-CERES adjustment. To fill the diurnal cycle beyond a solar zenith angle (SZA) of 82° and to fill missing time slots or faulty scan lines, we used CERES-SYN1deg-1hour data (Sec. 2c). Figure 6 shows the overall agreement between CERES-MODIS, GERB-SEVIRI, and CERES-SYN1deg-1hour data sets.

[Figure 6]

Resulting daily averages (Fig. 7) show significant flux differences between the equator and 40°S with a magnitude of 10 W m^{-2}. Regions of extreme differences line up with extremes in $\overline{R}_e$. For other days, differences were less pronounced or canceled out (not shown). As seen in Figure 6, daily mean differences can be traced back to GERB-based flux differences on the hourly time scale (e.g. for "Tropical Atlantic" between 1200-1400 UTC, or "Offshore" during most time slots). These were then amplified by CERES-based flux differences (e.g. for "Offshore" and "Tropical Atlantic") through GERB-to-CERES adjustment (see above). The region around 40°W, 20°N presents an example of similar cloud properties and yet flux differences of opposite sign that resulted from slightly different viewing geometries.

[Figure 7]

Finally, we computed monthly mean flux differences. Fewer areas show significant differences (Figs. 8 and 9). However, there are regions with significant difference in fluxes, up to 5 W m^{-2}. These regions are less coherent with extremes in $\overline{R}_e$ and $ACWV$. We presume that ranging sun-observer-geometries over the course of a months paired with ranging levels of $\overline{R}_e$ and $ACWV$ led to non-significant or vanishing flux differences.

[Figure 8 & 9]

For two selected pixels (marked in Fig. 7, 8, and 9) that showed significant differences in July, we plotted daily average scene properties and resulting flux differences (Fig. 10). "Coastal" (shown in red) was characterized by persistently low $\overline{R}_e$ and ranging $ACWV$, producing varying flux differences that were on average negative. "Offshore" (shown in blue), on the other hand, showed persistently low $ACWV$ and varying $\overline{R}_e$ that mostly resulted in positive differences and, thus, had a positive average difference. Monthly averages of strongly varying $\overline{R}_e$ and $ACWV$ (shown as triangles) resulted in non-extreme levels, while flux differences failed to cancel out towards vanishing monthly means.

[Figure 10]

In summary, we demonstrated that the choice of ADM matters for flux estimation in particular when encountering extremes in $\overline{R}_e$ and $ACWV$ and that can lead to instantaneous flux differences of up to 25 W m^{-2}. Instantaneous fluxes differed significantly when captured from the backscattering direction. Flux differences originating at the instantaneous level can lead to systematic differences in daily and monthly means on the order of 10 W m^{-2} and 5 W m^{-2}, respectively. Regions associated with significant differences were mainly closer to the continent or further offshore, where effective radii showed particularly small ($\overline{R}_e$<7μm) or large ($\overline{R}_e$>15μm) values, respectively.

4. Discussion

Angular distribution models allow to convert radiance observations from satellite platforms such as Aqua, Terra, or Meteosat 8 and 9 into outgoing radiative fluxes at TOA. A newly developed set of ADMs using semi-physical models (Tornow et al. 2020) offers a novel way to estimate solar fluxes over marine clouds. For liquid-phase clouds, we show here that instantaneous flux estimates from newly developed, semi-physical models may deviate up to 25 W m^{-2} from currently operational models employed in CERES SSF Edition 4A; given particularly small or large effective radii or loads of absorbing water vapor above clouds. We further demonstrate that these flux differences may occur systematically and affect daily and monthly means causing significant differences of the order of 10 W m-$^{-2}$ and 5 W m^{-2}, respectively.

Updated solar fluxes in regions of low-level clouds may improve our understanding of aerosol indirect effects and resulting radiative properties. Recent studies using instantaneous CERES SSF Edition 4 satellite observations to quantify the change in cloud radiative effects due to cloud-aerosol interaction (e.g. Painemal 2018; Gryspeerdt et al. 2019) may present less intense slopes using updated values of this study that indicated higher TOA SW fluxes for cloud of larger $\overline{R}_e$ and vice versa. The upcoming satellite mission EarthCARE (Illingworth et al. 2015) may also benefit from improved flux estimation. The mission is dedicated to assessing our current understanding of cloud-aerosol-radiation interaction by comparing observation-based TOA fluxes with radiative transfer calculations acting on cloud and aerosol retrievals from active-passive instruments. Scenes exhibiting solar or terrestrial flux differences beyond 10 W m^{-2} will be considered poorly understood. Mitigating hypothetical differences coming from the observation-based end (e.g. due to micro-physical extremes as seen in this study) will help narrowing the focus on scenes that deserve attention. Using ADMs that fail to produce adequate anisotropy responses to

$\overline{R}_e$ or $ACWV$, on the other hand, could cause > 10 W m^{-2} deviations over relatively straightforward Earth-atmospere scenes and may divert valuable resources by searching for possible insufficiencies in other parts of the closure assessment. Furthermore, data sets like CERES EBAF (Loeb et al. 2018) that rely on monthly means, as produced here, are crucial to evaluate the performance of climate models (e.g. Li et al. 2013; Ahlgrimm et al. 2018).

The physically plausible response of TOA SW anisotropy to $\overline{R}_e$ is evidence in favor for newly estimated fluxes being realistic. However, few instantaneous estimates could be identified as significantly different from currently operational estimates as error bars overlapped. The basis for uncertainty estimates were radiance residuals after fitting currently operational and newly developed, semi-physical models trying to capture all CERES-MODIS observations over a 5-year period. A case study using homogeneous samples of specific optical depth from this period dealt with much reduced radiance fluctuations and exhibited significant anisotropy differences (Tornow et al. 2018). We believe that the errors we estimate in this study (Sec. 2b) may have been too conservative and produced too large uncertainties for clouds of lower optical depth.

Daily mean differences between ADMs exceed other sources of uncertainty (Loeb et al. 2009), such as instrument calibration (2 W m^{-2}) or imperfect knowledge of solar irradiance (1 W m^{-2}). Additional uncertainty may originate from inaccurate retrievals of $ACWV$ (caused by cloud-top height retrieval or water vapor profiles) as well as $\overline{R}_e$. Systematic retrieval errors could be harmless if samples resemble the "training data" (here 5 years of CERES SSF observations) and if all viewing geometries for a selected illumination geometry are affected likewise. On the other hand, systematic errors could pose problems when predicting fluxes for other platforms (such as MSG satellites in this study). Future efforts need to ensure that SEVIRI retrieval of $\overline{R}_e$ and cloud-top height are consistent with CERES SSF data. Similarly, when switching to other sources for coincident profiles of atmospheric water vapor, cross-checks should be performed between the new source and the source used for training.

The response of TOA SW anisotropy to $ACWV$ was different than expected. Instead of a θ_v-dependency (expecting absorption to increase as the atmospheric mass grows with θ_v), we found dominant anisotropy sensitivity in the forward scattering direction (Fig. 1C), an angular portion associated with multi-scattering. We suspect that the observed response may have captured in-cloud absorption of multi-scattered sunlight and that could have served as proxy of in-cloud water vapor. These effects in the forward scattering direction may have clouded a θ_v-dependency that we found in simulated radiances (not shown). In this study, we found significant flux differences in regions that had low $ACWV$ values and little variation, and, therefore, can assume that we avoided potential anisotropy artifact. Future efforts should try to separate in-cloud from above-cloud absorption by e.g. introducing a single scattering albedo into the two-stream cloud albedo of newly developed, semi-physical models. This single scattering albedo ω could be a function of both $\overline{R}_e$ and in-cloud water vapor $ICWV$, $\omega = \omega(\overline{R}_e, ICWV)$.

With the advent of operational products reporting cloud-topped aerosol optical thickness (e.g. Peers et al. 2019; Sayer et al. 2016), the present semi-physical model could be readily expanded to incorporate absorption effects due to aerosol. Regions such as the southeast Atlantic experiencing seasonal plumes of biomass burning aerosol could be particularly benefiting from further refined models.

Finally, this study focused on liquid-phase clouds. We expect less flux differences for ice clouds as their $ACWV$ levels are much reduced and scattering effects on ice crystals (and their rich natural variety in shape treated as bulk) shows less marked changes with $\overline{R}_e$ (cf. Tornow et al. 2020). We do, however, expect differences for mixed-phase footprints (i.e. footprints which usually contain an ice cloud next to a liquid cloud) as their representation through newly developed, semi-physical models is more refined. Future work will carefully assess flux differences to the currently operational methodology.

Acknowledgments. The authors would like to thank HPC Service of ZEDAT (Freie Universität Berlin) for computing time, Wenying Su and Seiji Kato for their help to reproduce CERES angular distribution models, Nicolas Clerbaux, Jan Fokke Meirink, and Martin Stengel for scientific support with GERB and SEVIRI observations, and Allison McComiskey, Jens Redemann as well as colleagues at Institute for Space Sciences at Freie Universität Berlin and all other team members of the ESA project CLARA project for helpful discussion. We also thank three anonymous referees that helped to improve this manuscript substantially. We further thank the Atmospheric Sciences Data Center at the National Aeronautics and Space Administration Langley Research Center for providing the Clouds and Earth's Radiant Energy System Single Scanning Footprint TOA/Surface Fluxes and Clouds data product. This work was possible through funding within ESA Contract 4000112019/14/NL/CT.

Data availability statement. Data analyzed in this study were a re-analysis of existing data, which are openly available at locations cited in the reference section.

References

Ahlgrimm, M., R. M. Forbes, R. J. Hogan, and I. Sandu, 2018: Understanding Global Model Systematic Shortwave Radiation Errors in Subtropical Marine Boundary Layer Cloud Regimes. *Journal of Advances in Modeling Earth Systems*, **10 (8)**, 2042–2060, doi:10.1029/2018MS001346.

Barker, H. W., B. A. Wiellicki, and L. Parker, 1996: A Parameterization for Computing Grid-Averaged Solar Fluxes for Inhomogeneous Marine Boundary Layer Clouds. Part II: Validation

Using Satellite Data. *Journal of the Atmospheric Sciences*, **53 (16)**, 2304–2316, doi:10.1175/1520-0469(1996)053<2304:APFCGA>2.0.CO;2.

Barkstrom, B. R., 1990: Earth radiation budget measurements: pre-ERBE, ERBE, and CERES. *Long-Term Monitoring of the Earth's Radiation Budget*, B. R. Barkstrom, Ed., SPIE, International Society for Optics and Photonics, Vol. 1299, 52 – 60, doi:10.1117/12.21364.

Baum, B. A., P. Yang, A. J. Heymsfield, A. Bansemer, B. H. Cole, A. Merrelli, C. Schmitt, and C. Wang, 2014: Ice cloud single-scattering property models with the full phase matrix at wavelengths from 0.2 to 100μm. *Journal of Quantitative Spectroscopy and Radiative Transfer*, **146**, 123 – 139, doi:https://doi.org/10.1016/j.jqsrt.2014.02.029, electromagnetic and Light Scattering by Nonspherical Particles XIV.

Baum, B. A., P. Yang, A. J. Heymsfield, C. G. Schmitt, Y. Xie, A. Bansemer, Y.-X. Hu, and Z. Zhang, 2011: Improvements in Shortwave Bulk Scattering and Absorption Models for the Remote Sensing of Ice Clouds. *Journal of Applied Meteorology and Climatology*, **50 (5)**, 1037–1056, doi:10.1175/2010JAMC2608.1.

Benas, N., S. Finkensieper, M. Stengel, G.-J. van Zadelhoff, T. Hanschmann, R. Hollmann, and J. F. Meirink, 2017: The MSG-SEVIRI-based cloud property data record CLAAS-2. *Earth System Science Data*, **9 (2)**, 415–434, doi:10.5194/essd-9-415-2017.

Bender, F. A.-M., H. Rohde, R. J. Charlson, A. M. L. Ekman, and N. Loeb, 2006: 22 views of the global albedo—comparison between 20 GCMs and two satellites. *Tellus A*, **58 (3)**, 320–330, doi:10.1111/j.1600-0870.2006.00181.x.

Bennartz, R., and J. Fischer, 2000: A modified k-distribution approach applied to narrow band water vapour and oxygen absorption estimates in the near infrared. *Journal of Quantitative Spec-*

troscopy and Radiative Transfer, **66 (6)**, 539 – 553, doi:https://doi.org/10.1016/S0022-4073(99)00184-3.

Bennartz, R., and J. Rausch, 2017: Global and regional estimates of warm cloud droplet number concentration based on 13 years of aqua-modis observations. *Atmospheric Chemistry and Physics*, **17 (16)**, 9815–9836, doi:10.5194/acp-17-9815-2017, URL https://acp.copernicus.org/articles/17/9815/2017/.

Bolton, D., 1980: The Computation of Equivalent Potential Temperature. *Monthly Weather Review*, **108 (7)**, 1046–1053, doi:10.1175/1520-0493(1980)108<1046:TCOEPT>2.0.CO;2.

Bony, S., H. Le Treut, J.-P. Duvel, and R. S. Kandel, 1992: Satellite validation of GCM-simulated annual cycle of the earth radiation budget and cloud forcing. *Journal of Geophysical Research: Atmospheres*, **97 (D16)**, 18 061–18 081, doi:10.1029/92JD01631.

Brenguier, J.-L., H. Pawlowska, L. Schüller, R. Preusker, J. Fischer, and Y. Fouquart, 2000: Radiative Properties of Boundary Layer Clouds: Droplet Effective Radius versus Number Concentration. *Journal of the Atmospheric Sciences*, **57 (6)**, 803–821, doi:10.1175/1520-0469(2000)057<0803:RPOBLC>2.0.CO;2.

Cahalan, R. F., W. Ridgway, W. J. Wiscombe, T. L. Bell, and J. B. Snider, 1994: The Albedo of Fractal Stratocumulus Clouds. *Journal of the Atmospheric Sciences*, **51 (16)**, 2434–2455, doi:10.1175/1520-0469(1994)051<2434:TAOFSC>2.0.CO;2.

Cesana, G., A. D. Del Genio, and H. Chepfer, 2019: The cumulus and stratocumulus cloudsat-calipso dataset (casccad). *Earth System Science Data*, **11 (4)**, 1745–1764, doi:10.5194/essd-11-1745-2019, URL https://essd.copernicus.org/articles/11/1745/2019/.

Clough, S., M. Shephard, E. Mlawer, J. Delamere, M. Iacono, K. Cady-Pereira, S. Boukabara, and P. Brown, 2005: Atmospheric radiative transfer modeling: a summary of the AER codes. *Journal of Quantitative Spectroscopy and Radiative Transfer*, **91 (2)**, 233 – 244, doi:https://doi.org/10.1016/j.jqsrt.2004.05.058.

Cox, C., and W. Munk, 1954: Measurement of the Roughness of the Sea Surface from Photographs of the Sun's Glitter. *J. Opt. Soc. Am.*, **44 (11)**, 838–850, doi:10.1364/JOSA.44.000838.

Dewitte, S., and N. Clerbaux, 2017: Measurement of the Earth Radiation Budget at the Top of the Atmosphere—A Review. *Remote Sens.*, **9 (1143)**, 1–13, doi:10.3390/rs9111143.

Dewitte, S., L. Gonzalez, N. Clerbaux, A. Ipe, C. Bertrand, and B. D. Paepe], 2008: The Geostationary Earth Radiation Budget Edition 1 data processing algorithms. *Advances in Space Research*, **41 (11)**, 1906 – 1913, doi:https://doi.org/10.1016/j.asr.2007.07.042.

Diedrich, H., R. Preusker, R. Lindstrot, and J. Fischer, 2013: Quantification of uncertainties of water vapour column retrievals using future instruments. *Atmospheric Measurement Techniques*, **6 (2)**, 359–370, doi:10.5194/amt-6-359-2013.

Doelling, D., C. Haney, R. Bhatt, B. Scarino, and A. Gopalan, 2018: Geostationary Visible Imager Calibration for the CERES SYN1deg Edition 4 Product. *Remote Sensing*, **10 (288)**, doi:doi.org/10.3390/rs10020288.

Doelling, D. R., and Coauthors, 2013: Geostationary Enhanced Temporal Interpolation for CERES Flux Products. *Journal of Atmospheric and Oceanic Technology*, **30 (6)**, 1072–1090, doi:10.1175/JTECH-D-12-00136.1.

Finkensieper, S., and Coauthors, 2016: CLAAS-2: CM SAF CLoud property dAtAset using SEVIRI - Edition 2. *Satellite Application Facility on Climate Monitoring*, doi:10.5676/EUM_SAF_CM/CLAAS/V002.

Fu, Q., and K. N. Liou, 1992: On the Correlated k-Distribution Method for Radiative Transfer in Nonhomogeneous Atmospheres. *Journal of the Atmospheric Sciences*, **49 (22)**, 2139–2156, doi:10.1175/1520-0469(1992)049<2139:OTCDMF>2.0.CO;2.

Gao, M., X. Huang, P. Yang, and G. W. Kattawar, 2013: Angular distribution of diffuse reflectance from incoherent multiple scattering in turbid media. *Appl. Opt.*, **52 (24)**, 5869–5879, doi:10.1364/AO.52.005869.

Gristey, J. J., J. C. Chiu, R. J. Gurney, C. J. Morcrette, P. G. Hill, J. E. Russell, and H. E. Brindley, 2018: Insights into the diurnal cycle of global earth outgoing radiation using a numerical weather prediction model. *Atmospheric Chemistry and Physics*, **18 (7)**, 5129–5145, doi:10.5194/acp-18-5129-2018, URL https://acp.copernicus.org/articles/18/5129/2018/.

Gryspeerdt, E., and Coauthors, 2019: Constraining the aerosol influence on cloud liquid water path. *Atmospheric Chemistry and Physics*, **19 (8)**, 5331–5347, doi:10.5194/acp-19-5331-2019.

Hogan, R. J., M. D. Fielding, H. W. Barker, N. Villefranque, and S. A. K. Schäfer, 2019: Entrapment: An Important Mechanism to Explain the Shortwave 3D Radiative Effect of Clouds. *Journal of the Atmospheric Sciences*, **2019 (1)**, 48–66, doi:10.1175/JAS-D-18-0366.1.

Hollstein, A., and J. Fischer, 2012: Radiative transfer solutions for coupled atmosphere ocean systems using the matrix operator technique. *Journal of Quantitative Spectroscopy and Radiative Transfer*, **113 (7)**, 536 – 548, doi:https://doi.org/10.1016/j.jqsrt.2012.01.010.

Illingworth, A. J., and Coauthors, 2015: The EarthCARE Satellite: the next step forward in global measurements of clouds, aerosols, precipitation and radiation. *Bull. Am. Meteorol. Soc*, **96**, 1311–1332, doi:10.1175/BAMS-D-12-00227.1.

Ipe, A., C. Bertrand, N. Clerbaux, S. Dewitte, and L. Gonzalez, 2004: Validation and homogenization of cloud optical depth and cloud fraction retrievals for GERB/SEVIRI scene identification using Meteosat-7 data. *Atmospheric Research*, **72 (1)**, 17 – 37, doi:https://doi.org/10.1016/j.atmosres.2004.03.010, clouds and Radiation.

Li, J.-L. F., D. E. Waliser, G. Stephens, S. Lee, T. L'Ecuyer, S. Kato, N. Loeb, and H.-Y. Ma, 2013: Characterizing and understanding radiation budget biases in CMIP3/CMIP5 GCMs, contemporary GCM, and reanalysis. *Journal of Geophysical Research: Atmospheres*, **118 (15)**, 8166–8184, doi:10.1002/jgrd.50378.

Lilly, D. K., 1968: Models of cloud-topped mixed layers under a strong inversion. *Quarterly Journal of the Royal Meteorological Society*, **94 (401)**, 292–309, doi:10.1002/qj.49709440106, URL https://rmets.onlinelibrary.wiley.com/doi/abs/10.1002/qj.49709440106.

Lindstrot, R., R. Preusker, and J. Fischer, 2009: The Retrieval of Land Surface Pressure from MERIS Measurements in the Oxygen A Band. *Journal of Atmospheric and Oceanic Technology*, **26 (7)**, 1367–1377, doi:10.1175/2009JTECHA1212.1.

Loeb, N. G., S. Kato, K. Loukachine, and N. Manalo-Smith, 2005: Angular Distribution Models for Top-of-Atmosphere Radiative Flux Estimation from the Clouds and the Earth's Radiant Energy System Instrument on the Terra Satellite. Part I: Methodology. *Journal of Atmospheric and Oceanic Technology*, **22 (4)**, 338–351, doi:10.1175/JTECH1712.1.

Loeb, N. G., S. Kato, and B. A. Wielicki, 2002: Defining Top-of-the-Atmosphere Flux Reference Level for Earth Radiation Budget Studies. *Journal of Climate*, **15 (22)**, 3301–3309, doi:10.1175/1520-0442(2002)015<3301:DTOTAF>2.0.CO;2.

Loeb, N. G., N. Manalo-Smith, S. Kato, W. F. Miller, S. K. Gupta, P. Minnis, and B. A. Wielicki, 2003: Angular Distribution Models for Top-of-Atmosphere Radiative Flux Estimation from the Clouds and the Earth's Radiant Energy System Instrument on the Tropical Rainfall Measuring Mission Satellite. Part I: Methodology. *Journal of Applied Meteorology*, **42 (2)**, 240–265, doi:10.1175/1520-0450(2003)042<0240:ADMFTO>2.0.CO;2.

Loeb, N. G., B. A. Wielicki, D. R. Doelling, G. L. Smith, D. F. Keyes, S. Kato, N. Manalo-Smith, and T. Wong, 2009: Toward Optimal Closure of the Earth's Top-of-Atmosphere Radiation Budget. *Journal of Climate*, **22 (3)**, 748–766.

Loeb, N. G., and Coauthors, 2018: Clouds and the Earth's Radiant Energy System (CERES) Energy Balanced and Filled (EBAF) Top-of-Atmosphere (TOA) Edition-4.0 Data Product. *Journal of Climate*, **31 (2)**, 895–918, doi:10.1175/JCLI-D-17-0208.1.

Painemal, D., 2018: Global Estimates of Changes in Shortwave Low-Cloud Albedo and Fluxes Due to Variations in Cloud Droplet Number Concentration Derived From CERES-MODIS Satellite Sensors. *Geophysical Research Letters*, **45 (17)**, 9288–9296, doi:10.1029/2018GL078880.

Painemal, D., S. Kato, and P. Minnis, 2014: Boundary layer regulation in the southeast atlantic cloud microphysics during the biomass burning season as seen by the a-train satellite constellation. *Journal of Geophysical Research: Atmospheres*, **119 (19)**, 11,288–11,302, doi:10.1002/2014JD022182, URL https://agupubs.onlinelibrary.wiley.com/doi/abs/10.1002/2014JD022182.

Peers, F., and Coauthors, 2019: Observation of absorbing aerosols above clouds over the south-east atlantic ocean from the geostationary satellite seviri – part 1: Method description and sensitivity. *Atmospheric Chemistry and Physics*, **19 (14)**, 9595–9611, doi:10.5194/acp-19-9595-2019, URL https://acp.copernicus.org/articles/19/9595/2019/.

Pincus, R., H. W. Barker, and J.-J. Morcrette, 2003: A fast, flexible, approximate technique for computing radiative transfer in inhomogeneous cloud fields. *Journal of Geophysical Research: Atmospheres*, **108 (D13)**, doi:10.1029/2002JD003322.

Poli, P., and Coauthors, 2016: ERA-20C: An Atmospheric Reanalysis of the Twentieth Century. *Journal of Climate*, **29 (11)**, 4083–4097, doi:10.1175/JCLI-D-15-0556.1.

Ramanathan, V., 1987: The role of earth radiation budget studies in climate and general circulation research. *Journal of Geophysical Research: Atmospheres*, **92 (D4)**, 4075–4095, doi:10.1029/JD092iD04p04075.

Rienecker, M. M., M. J. Suarez, R. Todling, J. Bacmeister, L. Takacs, H.-C. Liu, W. Gu, and M. Sienkiewicz, 2008: The GOES-5 Data Assimilation System—Documentation of versions 5.0.1, 5.1.0, and 5.2.0. Tech. rep., NASA. URL https://ntrs.nasa.gov/archive/nasa/casi.ntrs.nasa.gov/20120011955.pdf, series on Global Modeling and Data Assimilation NASA/TM-2008-104606.

Rothman, L., and Coauthors, 2009: The HITRAN 2008 molecular spectroscopic database. *Journal of Quantitative Spectroscopy and Radiative Transfer*, **110 (9)**, 533 – 572, doi:https://doi.org/10.1016/j.jqsrt.2009.02.013, hITRAN.

Rutan, D. A., G. L. Smith, and T. Wong, 2014: Diurnal Variations of Albedo Retrieved from Earth Radiation Budget Experiment Measurements. *Journal of Applied Meteorology and Cli-*

matology, **53 (12)**, 2747–2760, doi:10.1175/JAMC-D-13-0119.1, URL https://doi.org/10.1175/JAMC-D-13-0119.1.

Sayer, A. M., N. C. Hsu, C. Bettenhausen, J. Lee, J. Redemann, B. Schmid, and Y. Shinozuka, 2016: Extending "deep blue" aerosol retrieval coverage to cases of absorbing aerosols above clouds: Sensitivity analysis and first case studies. *Journal of Geophysical Research: Atmospheres*, **121 (9)**, 4830–4854, doi:https://doi.org/10.1002/2015JD024729, URL https://agupubs.onlinelibrary.wiley.com/doi/abs/10.1002/2015JD024729.

Smith, G., K. Priestley, N. Loeb, B. Wielicki, T. Charlock, P. Minnis, D. Doelling, and D. Rutan, 2011: Clouds and earth radiant energy system (ceres), a review: Past, present and future. *Advances in Space Research*, **48 (2)**, 254 – 263, doi:https://doi.org/10.1016/j.asr.2011.03.009, URL http://www.sciencedirect.com/science/article/pii/S0273117711001700.

Smith, G. L., R. N. Green, E. Raschke, L. M. Avis, J. T. Suttles, B. A. Wielicki, and R. Davies, 1986: Inversion methods for satellite studies of the Earth's Radiation Budget: Development of algorithms for the ERBE Mission. *Reviews of Geophysics*, **24 (2)**, 407–421, doi:10.1029/RG024i002p00407.

Su, W., J. Corbett, Z. Eitzen, and L. Liang, 2015: Next-generation angular distribution models for top-of-atmosphere radiative flux calculation from CERES instruments: methodology. *Atmospheric Measurement Techniques*, **8 (2)**, 611–632, doi:10.5194/amt-8-611-2015.

Suttles, J. T., and Coauthors, 1988: Angular radiation models for Earth-atmosphere system, Vol. I, Shortwave radiation. Tech. rep., NASA Langley Research Center, Hampton, Virginia. NASA RP-1184.

Toll, V., M. Christensen, S. Gassó, and N. Bellouin, 2017: Volcano and ship tracks indicate excessive aerosol-induced cloud water increases in a climate model. *Geophysical Research Letters*, **44 (24)**, 12,492–12,500, doi:10.1002/2017GL075280, URL https://agupubs.onlinelibrary.wiley.com/doi/abs/10.1002/2017GL075280.

Tornow, F., C. Domenech, H. W. Barker, R. Preusker, and J. Fischer, 2020: Using Two-Stream Theory to Capture Fluctuations of Satellite-Perceived TOA SW Radiances Reflected from Clouds over Ocean. *Atmospheric Measurement Techniques Discussions*, 1–21, doi:10.5194/amt-2020-149.

Tornow, F., R. Preusker, C. Domenech, C. K. Carbajal Henken, S. Testorp, and J. Fischer, 2018: Top-of-Atmosphere Shortwave Anisotropy over Liquid Clouds: Sensitivity to Clouds' Microphysical Structure and Cloud-Topped Moisture. *Atmosphere*, **9 (7)**, doi:10.3390/atmos9070256, URL https://www.mdpi.com/2073-4433/9/7/256.

Twomey, S., 1977: The Influence of Pollution on the Shortwave Albedo of Clouds. *Journal of the Atmospheric Sciences*, **34 (7)**, 1149–1152, doi:10.1175/1520-0469(1977)034<1149:TIOPOT>2.0.CO;2.

Wielicki, B. A., B. R. Barkstrom, E. F. Harrison, R. B. L. III, G. L. Smith, and J. E. Cooper, 1996: Clouds and the Earth's Radiant Energy System (CERES): An Earth Observing System Experiment. *Bulletin of the American Meteorological Society*, **77 (5)**, 853–868, doi:10.1175/1520-0477(1996)077<0853:CATERE>2.0.CO;2.

Wood, R., 2012: Stratocumulus Clouds. *Monthly Weather Review*, **140 (8)**, 2373–2423, doi:10.1175/MWR-D-11-00121.1, URL https://doi.org/10.1175/MWR-D-11-00121.1, https://journals.ametsoc.org/mwr/article-pdf/140/8/2373/4279106/mwr-d-11-00121_1.pdf.

LIST OF FIGURES

Fig. 1. Along the principal plane of solar geometry $\theta_0 \in [32,34°]$, we present the response of TOA SW anisotropy to newly introduced parameters of semi-physical ADMs (shown in colors) and comparison to currently operational ADMs (shown in black) that were insensitive to these parameters. Negative x-values correspond to the backscattering direction ($\varphi \in [178,180°]$), while positive values mark the forwardscattering direction ($\varphi \in [0,2°]$). Panels I and II present the response of two cloud scenarios to ranging $\bar{R}_e$, and panel III of a third scenario to ranging $ACWV$. Uncertainties, shown in error bars for semi-physical ADMs and as grey shading for currently operational ones, were derived as explained in Sec. 2b. Note the changing limits of y-axes across panels. 36

Fig. 2. Anisotropy changes in newly developed, semi-physical ADMs (triangles) over varying $\bar{R}_e$ and $ACWV$ (left and right side, respectively) which currently operational ADMs (circles) were insensitive to. For two $\tilde{\tau}$ (separated by linetype) and three viewing geometries (indicated by color, and of following specific geometry: direct backscatter - $\varphi \in [178,180°]$, $\theta_v \in [32,34°]$; forwardscatter - $\varphi \in [0,2°]$, $\theta_v \in [68,70°]$; nadir - $\theta_v \in [0,2°]$) and a constant solar geometry of $\theta_0 \in [32,34°]$, we hightlight for which $\bar{R}_e$ and $ACWV$ both ADMs agree. Bottom plots show histograms of respective variable over three $\tilde{\tau}$-ranges and help understanding potential sampling biases in currently operational ADMs. 37

Fig. 3. The theoretic deviation when estimating fluxes with newly developed, semi-physical rather than currently operational ADMs, shown for two liquid-cloud cases (vertically, specified on the right side, both of 100% cloud fraction) and for three scenarios of cloud effective radii (horizontal direction, specified on the top). Deviations were determined as defined in Equ. 15. Values beyond ±15 W m^{-}2 were not resolved and are shown as darkest colours. Plus signs and asteriks mark the center of Sun glint and direct backscattering, respectively. . . 38

Fig. 4. Quantifying the upper bound of deviations in fluxes $\delta\hat{F}_{max}$ when using newly developed, semi-physical over currently operational ADMs. To approximate upper bounds, we assumed extremes of newly added parameters to be $\bar{R}_e$ (5 and 20 µm) and $ACWV$ (0 and 20 kg m^{-2}), drawing from observed probability densitites shown in Fig. 2. We quantified flux deviations as defined in Equation 16 and per cloud optical depth and solar geometry. 39

Fig. 5. Exemplary application of both newly developed, semi-physical and currently operational ADMs to GERB-SEVIRI observations onboard Meteosat Second Generation satellites as well CERES-MODIS observations onboard Aqua and Terra satellites. Values were gridded onto an equal-area grid (as defined in Doelling et al. 2013). From left to right, we present TOA SW fluxes based on CERES ADMs, flux deviations between both ADMs, and corresponding imager-retrieved scene properties $\bar{R}_e$, $\tilde{\tau}$, and f. 40

Fig. 6. Details of diurnal observations for three selected pixels (by column). From top to bottom, we show flux estimates, solar geometry, and gridded scene properties f, $\tilde{\tau}$, and $\overline{R_e}$. As specified in the legend, this composition contains values from CERES-MODIS, GERB-SEVIRI, and CERES-SYN1deg-1hour. 41

Fig. 7. The daily average for July 6th 2007. The panel on the left shows the difference in daily average fluxes based on newly developed, semi-physical model minus currently operational approach. In smaller panels from top-left to bottom-right are shown daily average of fluxes from currently operational approach, effective cloud particle size, cloud optical depth, above-cloud water vapor, cloud phase, and cloud fraction. Insignificant values of the panel on the left are presented dashed and were determined via two-sided Student's t-test using paired hourly

flux estimates from semi-physical and currently operational ADMs at the 90% confidence level. 42

Fig. 8. A monthly average for January 2007. Panels and their variables correpond to Fig. 7. Like daily averages, we performed the Student's t-test using paired daily averages based on each newly developed, semi-physical and currently operational ADMs and a 90% confidence level . 43

Fig. 9. In line with Fig. 8, we show a monthly average for July 2007. 44

Fig. 10. Daily averages during the month of July 2007 for two selected pixels (separated by color). We show differences in daily mean fluxes (errorbars show the standard error), and daily mean $\tilde{\tau}$, $\bar{R}_e$, and $ACWV$ (from top to bottom). Triangles on the right mark monthly mean and histograms on the far right capture the spread of daily means over the month. 45

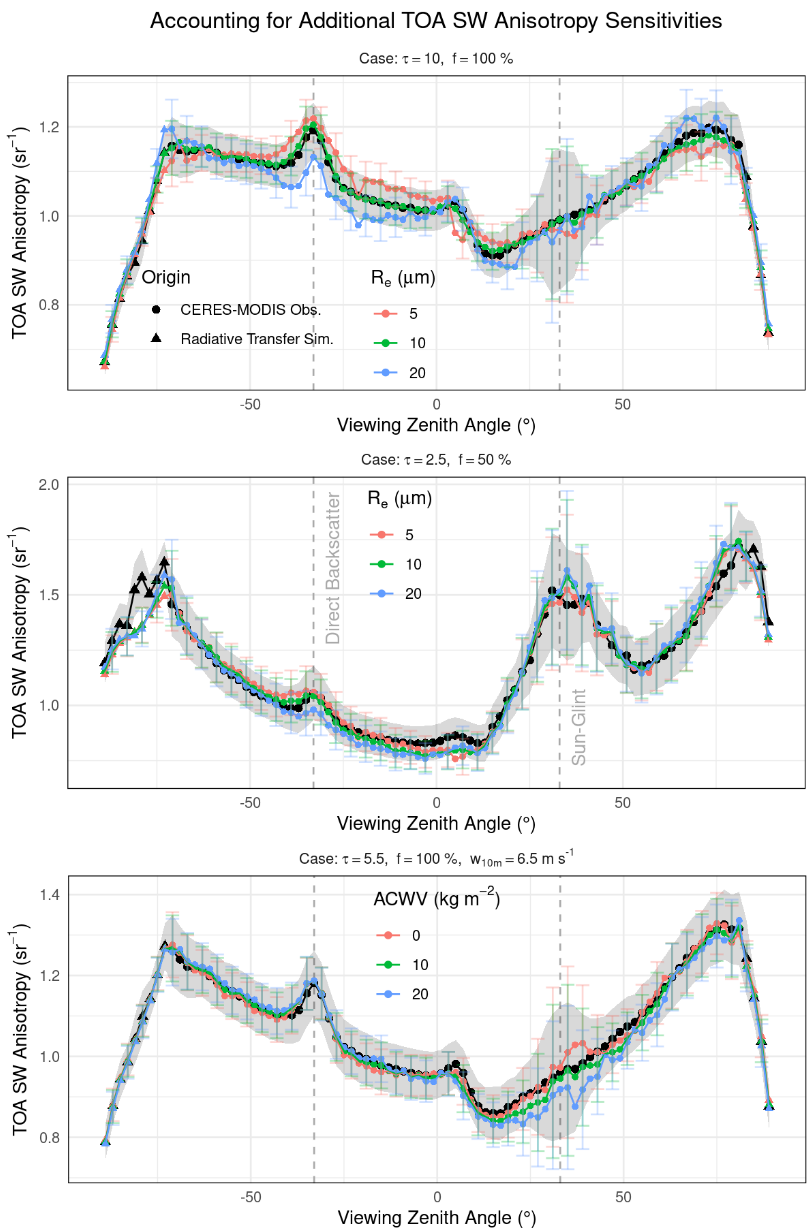

FIG. 1. Along the principal plane of solar geometry $\theta_0 \in [32, 34°]$, we present the response of TOA SW anisotropy to newly introduced parameters of semi-physical ADMs (shown in colors) and comparison to currently operational ADMs (shown in black) that were insensitive to these parameters. Negative x-values correspond to the backscattering direction ($\varphi \in [178, 180°]$), while positive values mark the forwardscattering direction ($\varphi \in [0, 2°]$). Panels I and II present the response of two cloud scenarios to ranging $\bar{R}_e$, and panel III of a third scenario to ranging $ACWV$. Uncertainties, shown in error bars for semi-physical ADMs and as grey shading for currently operational ones, were derived as explained in Sec. 2b. Note the changing limits of y-axes across panels.

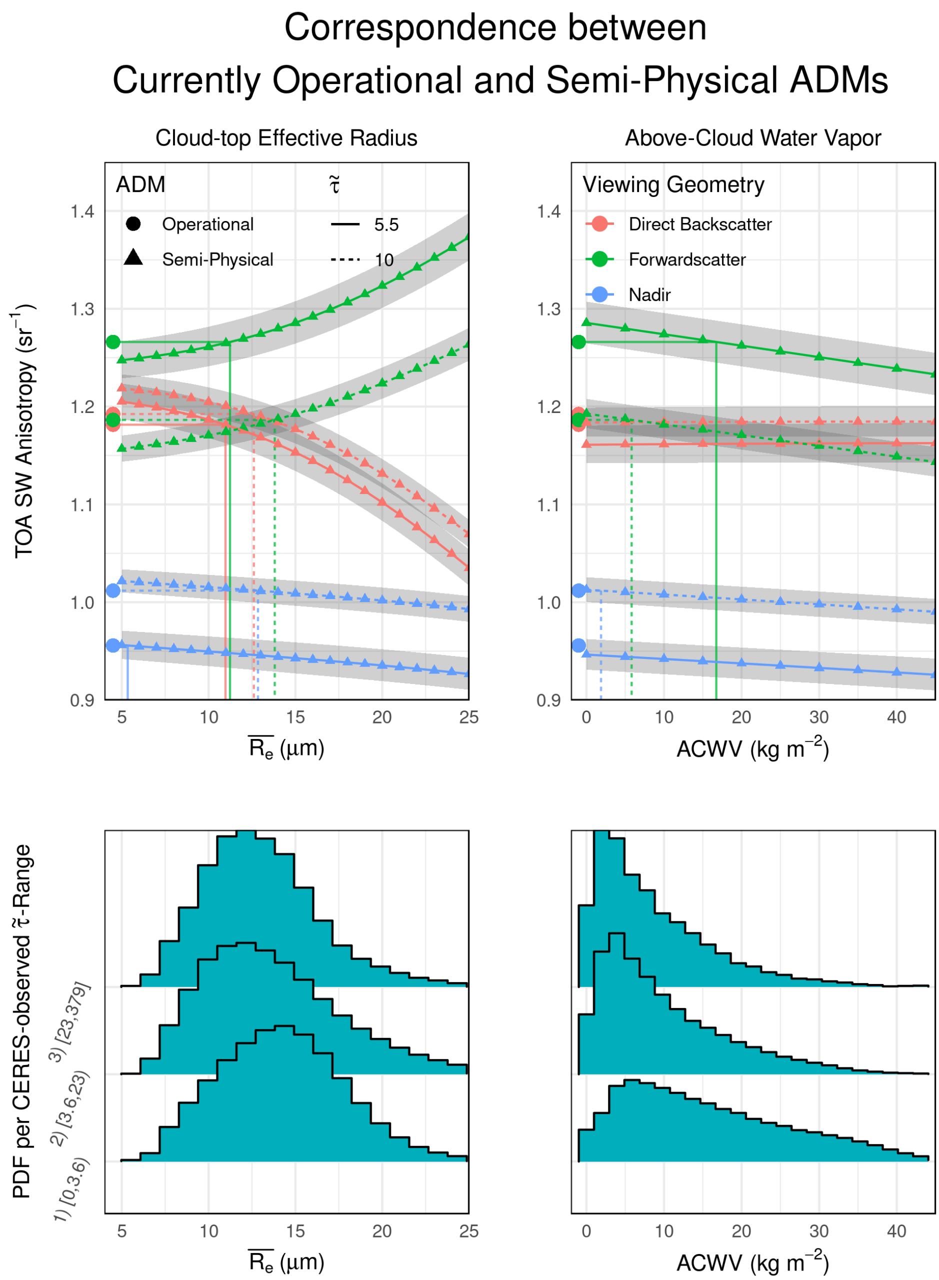

Fig. 2. Anisotropy changes in newly developed, semi-physical ADMs (triangles) over varying $\bar{R}_e$ and $ACWV$ (left and right side, respectively) which currently operational ADMs (circles) were insensitive to. For two $\tilde{\tau}$ (separated by linetype) and three viewing geometries (indicated by color, and of following specific geometry: direct backscatter - $\varphi \in [178, 180°]$, $\theta_v \in [32, 34°]$; forwardscatter - $\varphi \in [0, 2°]$, $\theta_v \in [68, 70°]$; nadir - $\theta_v \in [0, 2°]$) and a constant solar geometry of $\theta_0 \in [32, 34°]$, we hightlight for which $\bar{R}_e$ and $ACWV$ both ADMs agree. Bottom plots show histograms of respective variable over three $\tilde{\tau}$-ranges and help understanding potential sampling biases in currently operational ADMs.

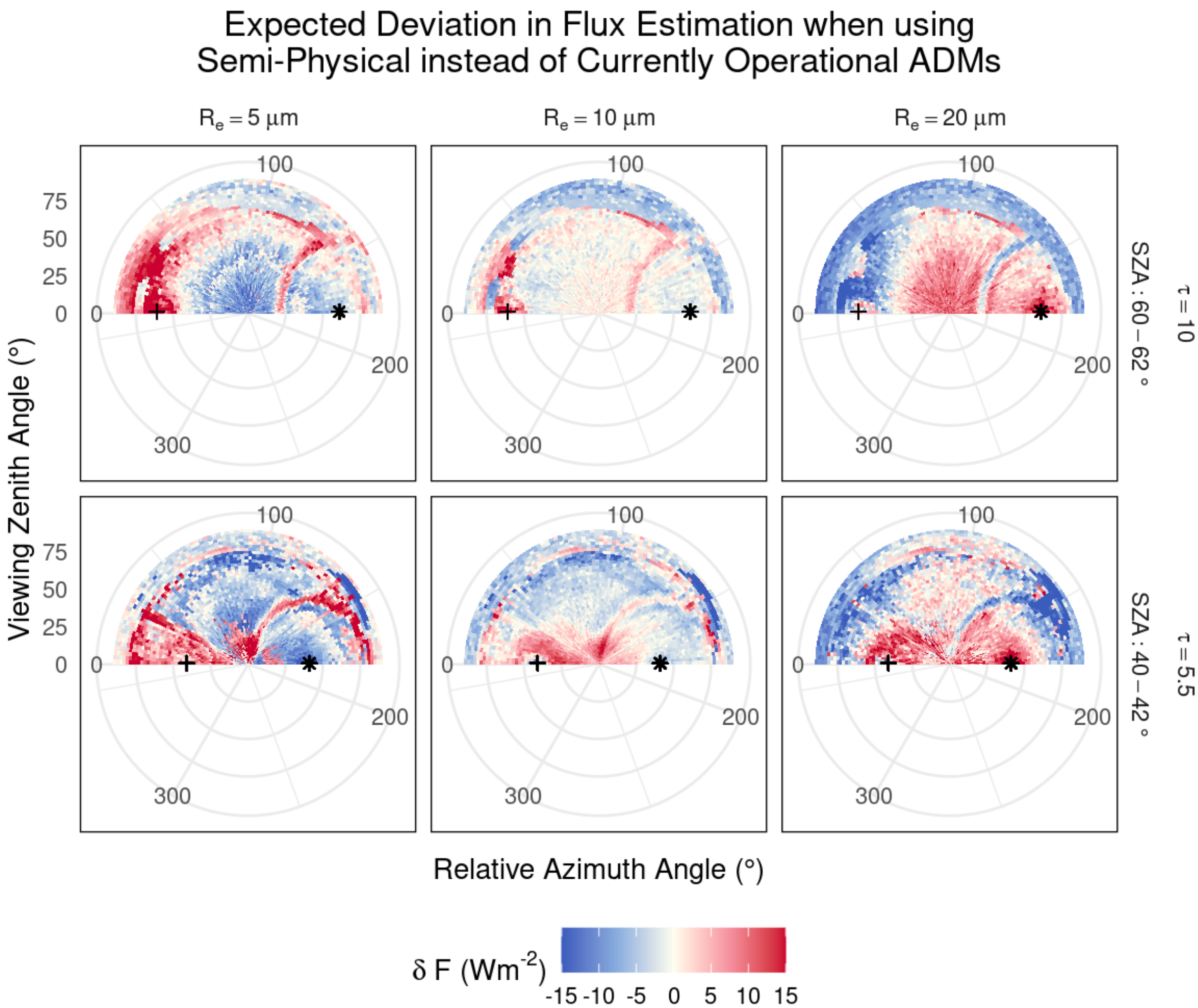

FIG. 3. The theoretic deviation when estimating fluxes with newly developed, semi-physical rather than currently operational ADMs, shown for two liquid-cloud cases (vertically, specified on the right side, both of 100% cloud fraction) and for three scenarios of cloud effective radii (horizontal direction, specified on the top). Deviations were determined as defined in Equ. 15. Values beyond ±15 W m^{-}2 were not resolved and are shown as darkest colours. Plus signs and asteriks mark the center of Sun glint and direct backscattering, respectively.

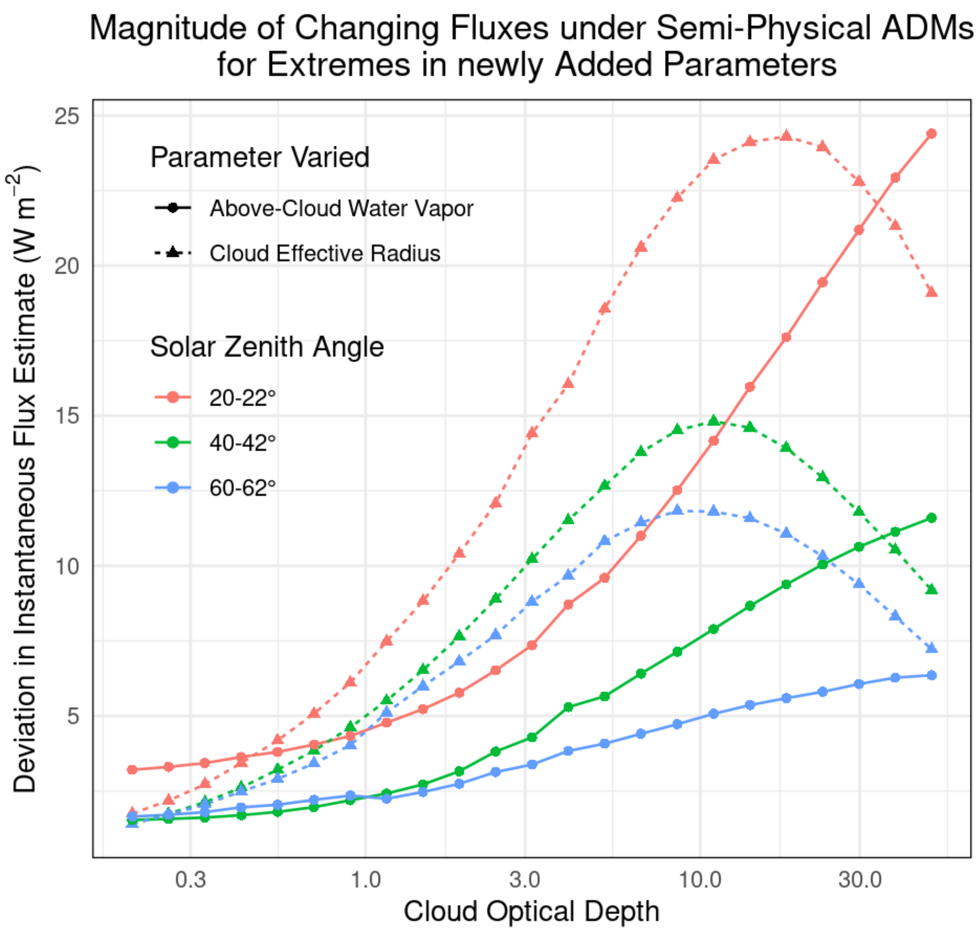

Fig. 4. Quantifying the upper bound of deviations in fluxes $\delta\hat{F}_{max}$ when using newly developed, semi-physical over currently operational ADMs. To approximate upper bounds, we assumed extremes of newly added parameters to be $\bar{R}_e$ (5 and 20 μm) and $ACWV$ (0 and 20 kg m^{-2}), drawing from observed probability densitites shown in Fig. 2. We quantified flux deviations as defined in Equation 16 and per cloud optical depth and solar geometry.

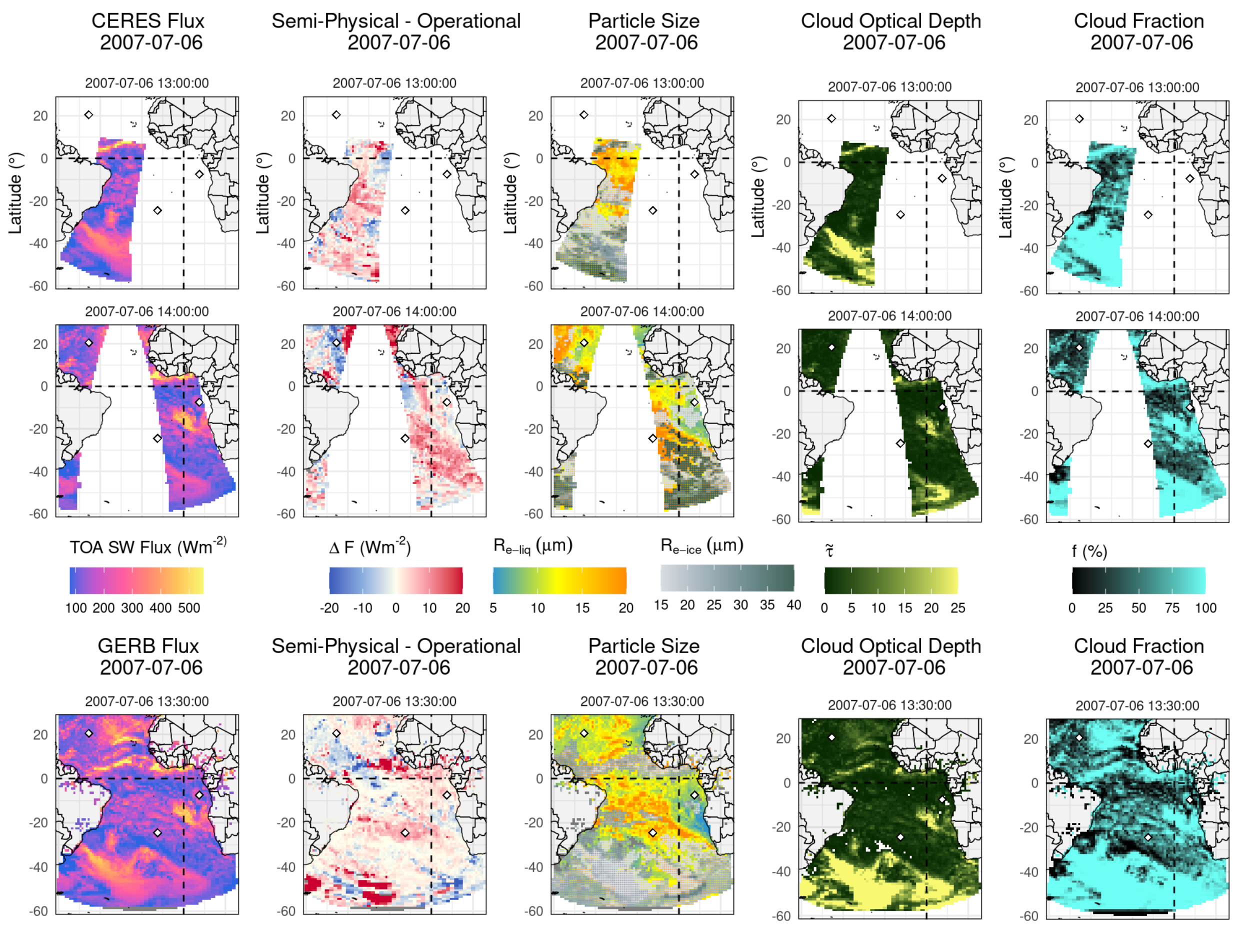

FIG. 5. Exemplary application of both newly developed, semi-physical and currently operational ADMs to GERB-SEVIRI observations onboard Meteosat Second Generation satellites as well CERES-MODIS observations onboard Aqua and Terra satellites. Values were gridded onto an equal-area grid (as defined in Doelling et al. 2013). From left to right, we present TOA SW fluxes based on CERES ADMs, flux deviations between both ADMs, and corresponding imager-retrieved scene properties $\bar{R}_e$, $\tilde{\tau}$, and f.

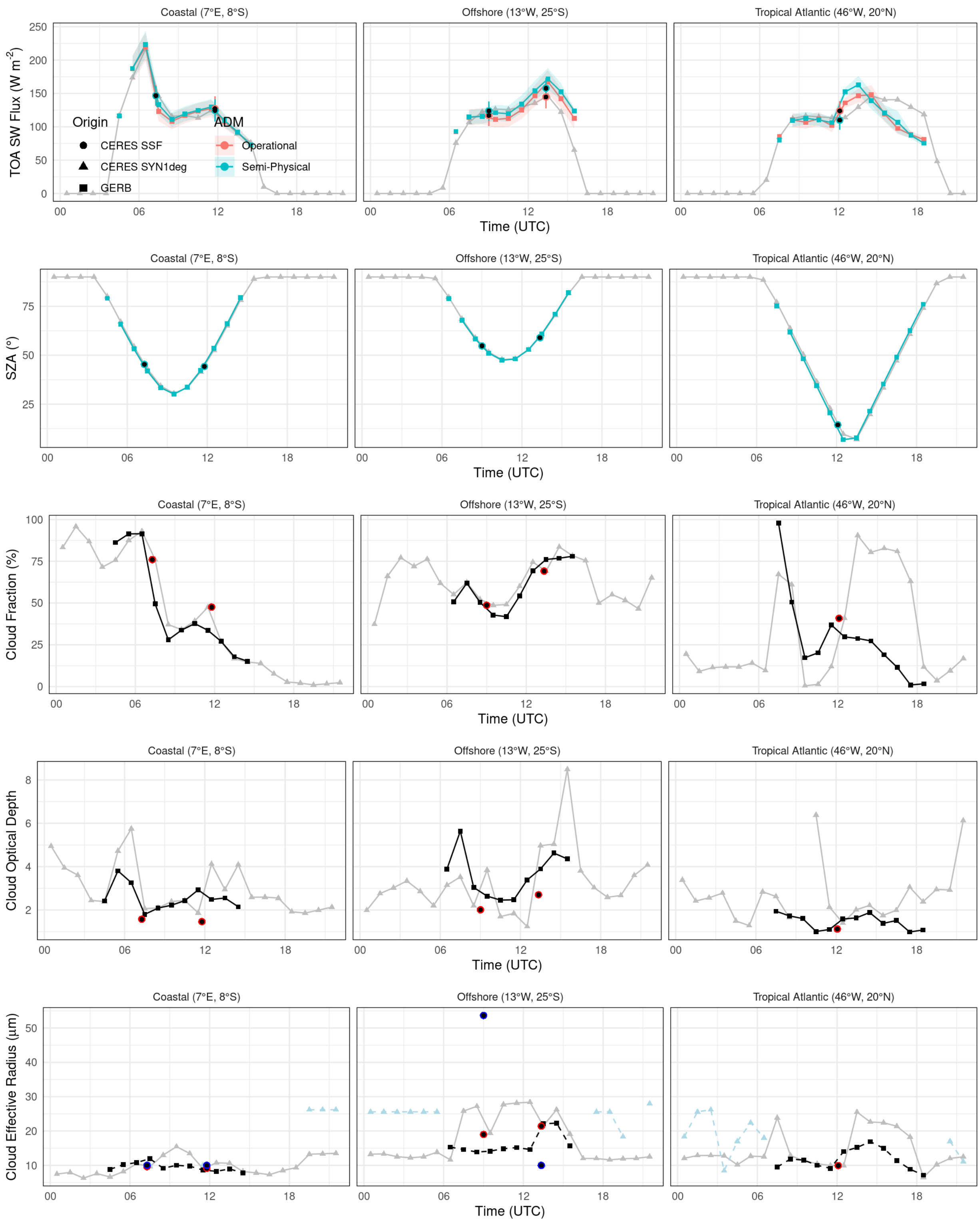

783 FIG. 6. Details of diurnal observations for three selected pixels (by column). From top to bottom, we show flux

784 estimates, solar geometry, and gridded scene properties f, $\tilde{\tau}$, and $\overline{R}_e$. As specified in the legend, this composition

785 contains values from CERES-MODIS, GERB-SEVIRI, and CERES-SYN1deg-1hour.

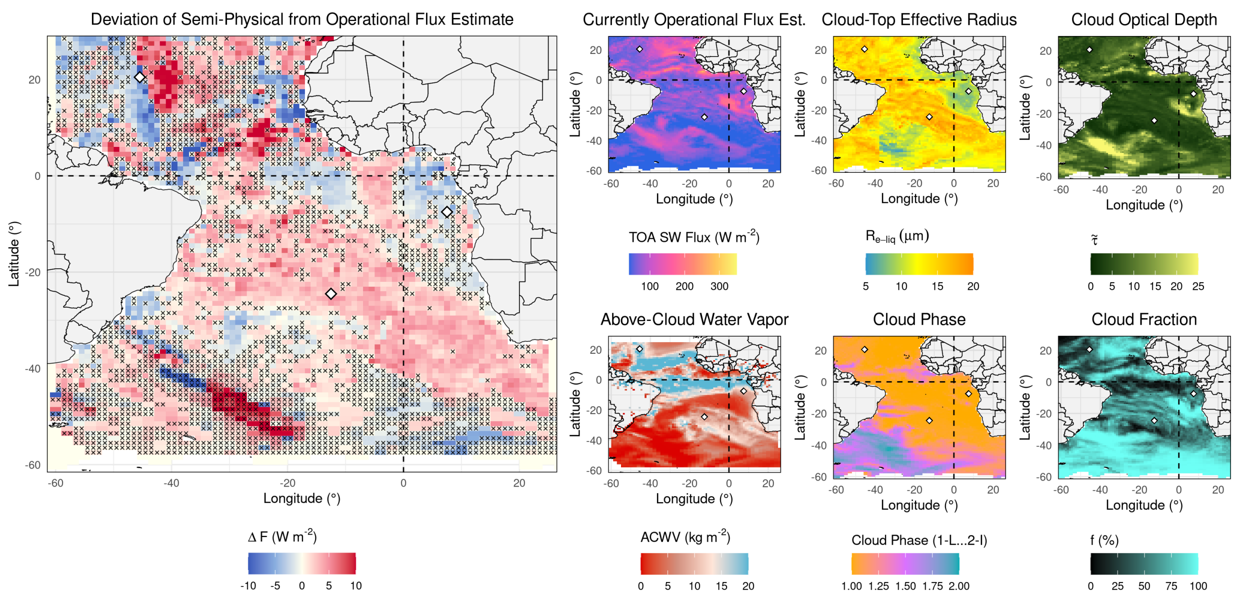

FIG. 7. The daily average for July 6th 2007. The panel on the left shows the difference in daily average fluxes based on newly developed, semi-physical model minus currently operational approach. In smaller panels from top-left to bottom-right are shown daily average of fluxes from currently operational approach, effective cloud particle size, cloud optical depth, above-cloud water vapor, cloud phase, and cloud fraction. Insignificant values of the panel on the left are presented dashed and were determined via two-sided Student's t-test using paired hourly flux estimates from semi-physical and currently operational ADMs at the 90% confidence level.

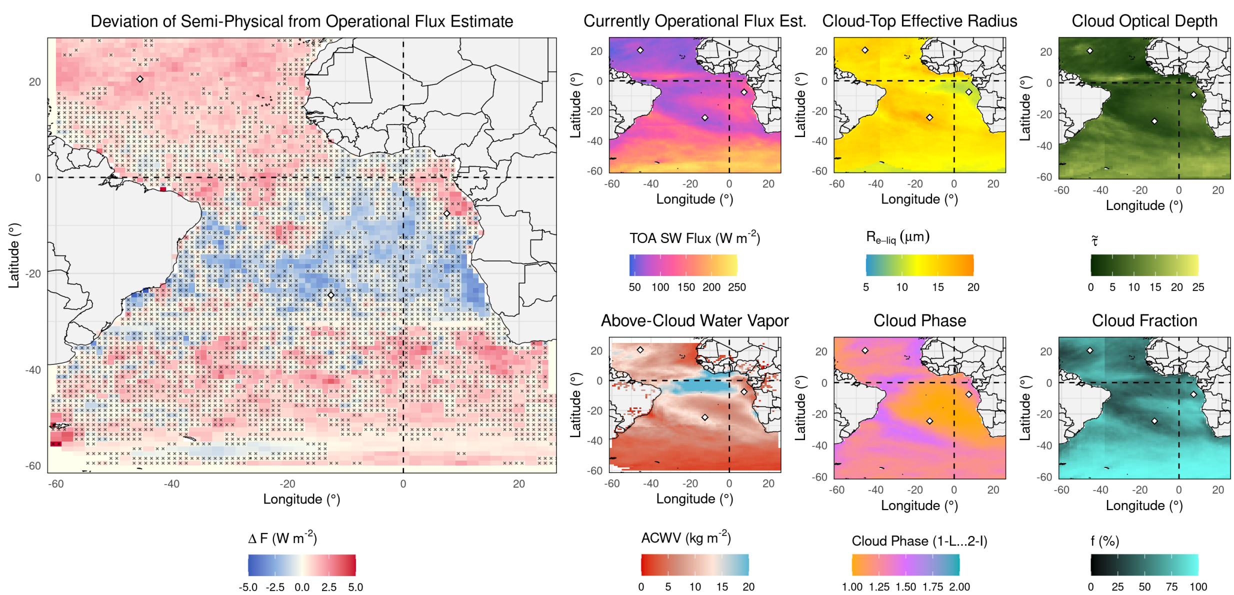

FIG. 8. A monthly average for January 2007. Panels and their variables correpond to Fig. 7. Like daily averages, we performed the Student's t-test using paired daily averages based on each newly developed, semi-physical and currently operational ADMs and a 90% confidence level

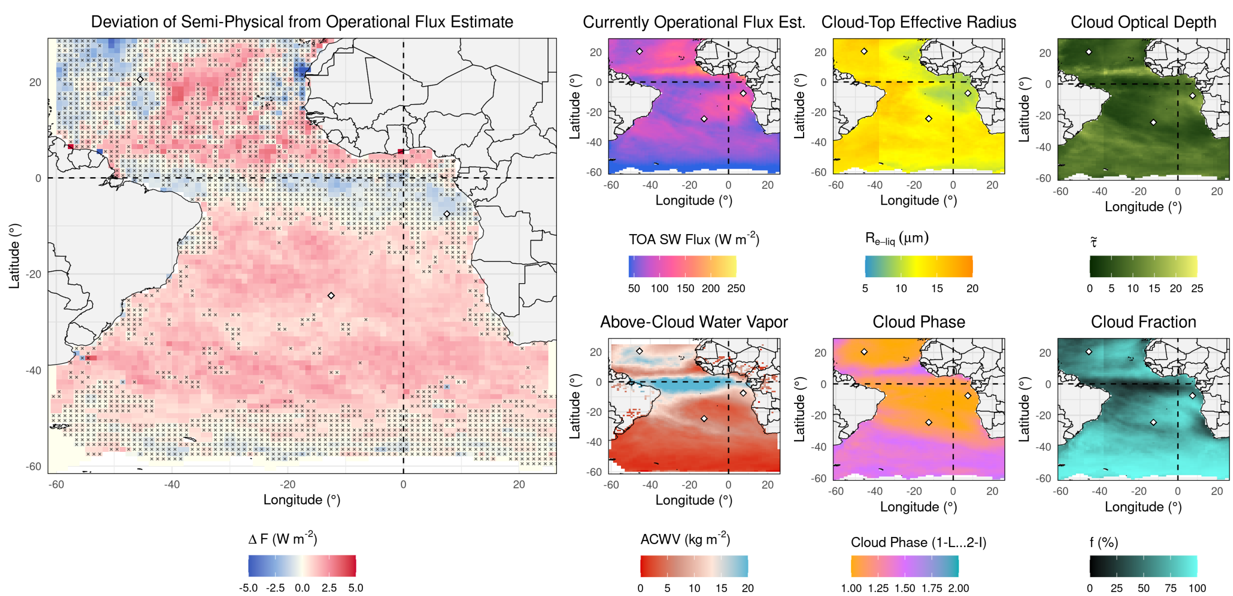

FIG. 9. In line with Fig. 8, we show a monthly average for July 2007.

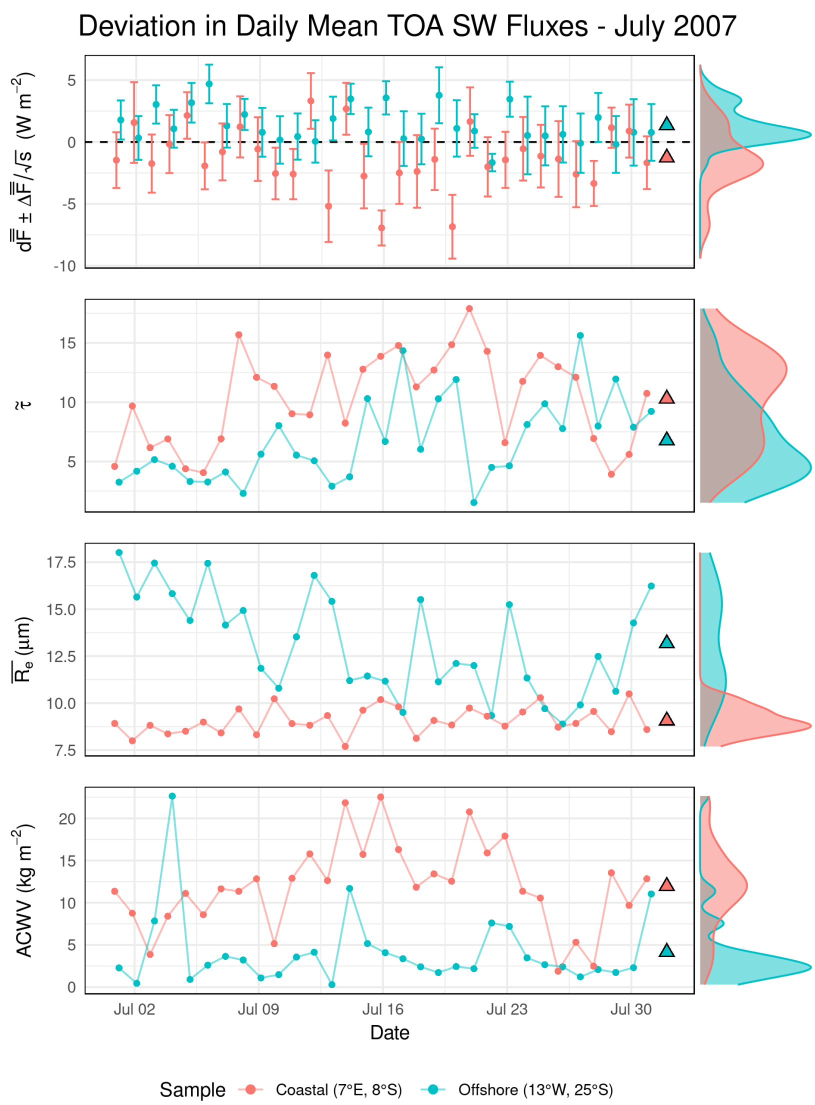

795 FIG. 10. Daily averages during the month of July 2007 for two selected pixels (separated by color). We show
796 differences in daily mean fluxes (errorbars show the standard error), and daily mean $\tilde{\tau}$, $\bar{R}_e$, and $ACWV$ (from top
797 to bottom). Triangles on the right mark monthly mean and histograms on the far right capture the spread of daily
798 means over the month.